Nanoscale

PAPER

View Article Online
View Journal | View Issue

Cite this: *Nanoscale*, 2019, **11**, 10097

Sulfur impregnation in polypyrrole-modified MnO_2 nanotubes: efficient polysulfide adsorption for improved lithium–sulfur battery performance†

Pengcheng Du, *‡[a] Wenli Wei,‡[a,b] Yuman Dong,‡[a] Dong Liu,[a] Qi Wang,[a] Yi Peng,[b] Shaowei Chen *[b] and Peng Liu *[a]

Received 22nd December 2018,
Accepted 8th May 2019

DOI: 10.1039/c8nr10353d

rsc.li/nanoscale

Rechargeable lithium–sulfur batteries have emerged as a viable technology for next generation electrochemical energy storage, and the sulfur cathode plays a critical role in determining the device performance. In this study, we prepared functional composites based on polypyrrole-coated MnO_2 nanotubes as a highly efficient sulfur host (sulfur mass loading 63.5%). The hollow interior of the MnO_2 nanotubes not only allowed for accommodation of volumetric changes of sulfur particles during the cycling process, but also confined the diffusion of lithium polysulfides by physical restriction and chemical adsorption, which minimized the loss of polysulfide species. In addition, the polypyrrole outer layer effectively enhanced the electrical conductivity of the cathode to facilitate ion and electron transport. The as-prepared MnO_2-PPy-S composite delivered an initial specific capacity of 1469 mA h g^{-1} and maintained an extremely stable cycling performance, with a small capacity decay of merely 0.07% per cycle at 0.2C within 500 cycles, a high average coulombic efficiency of 95.7% and an excellent rate capability at 470 mA h g^{-1} at the current density of 3C.

1. Introduction

Lithium sulfur batteries (LSB) have been attracting extensive interest as a promising next-generation high energy storage technology, due to the high theoretical specific capacity, low costs and environmental friendliness of the electrode materials.[1–4] Sulfur has been known to undergo multi-electron reactions with Li ions and exhibit a high theoretical specific capacity of 1672 mA h g^{-1}.[4] Ideally, the cathode materials for LSB should include a high surface area and large pore volume to accommodate a high loading of sulfur particles, strong polar absorption for soluble reactive intermediates, and highly conductive network for rapid transport of ions and electrons.[5] However, the performance of LSB has been limited by several challenging obstacles, such as fast capacity decay, low coulombic efficiency and poor rate capability, which greatly hinder the practical applications.[3,4] These issues are mainly ascribed to the low electrical conductivity of the active materials (*e.g.*, sulfur, Li_2S, and Li_2S_2), diffusion (and loss) of soluble polysulfide intermediates, and large volumetric changes of the cathode materials during the charge–discharge process.[6]

These issues may be mitigated by the development of new, effective sulfur hosts,[7,8] modification of membrane surfaces,[9–11] and/or addition of electrolyte additives.[12,13] In a number of studies, conductive matrices, such as carbon materials and conductive polymers, have been employed to encapsulate sulfur, improve electrical conductivity of the cathode as well as minimize the loss of lithium polysulfides.[14,15] In particular, carbon materials with a high specific surface area and large pore volume have been used rather extensively, such as meso/microporous carbons,[16] graphene,[7,17–19] hollow carbon nanofibers,[20] hollow carbon nanospheres,[21] and carbon nanotubes.[22,23] In addition, conductive polymers, such as polypyrrole (PPy),[24] polyaniline (PANI)[25] and poly(3,4-ethylenedioxythiophne) (PEDOT),[8,26] have also been used to host sulfur particles. The resulting sulfur-encapsulated nanocomposites typically exhibit enhanced specific capacity and good cycling performance during the initial cycles. But the coulombic efficiency in general remains low, and rapid capacity loss occurs during long-term cycling, as the non-polar carbon/polymer hosts cannot efficiently entrap the polar lithium polysulfide species because of weak interactions with sulfur.

Polar host materials, such as metal oxides of TiO_2,[27] MnO_2,[28] γ-Fe_2O_3,[29] V_2O_5,[30] MgO,[31] metal hydroxides of $Ni(OH)_2$,[32] and metal–organic frameworks (MOFs),[33,34] have

[a]*State Key Laboratory of Applied Organic Chemistry and Institute of Polymer Science and Engineering, College of Chemistry and Chemical Engineering, Lanzhou University, Lanzhou 730000, People's Republic of China. E-mail: dupch@lzu.edu.cn, pliu@lzu.edu.cn*

[b]*Department of Chemistry and Biochemistry, University of California, 1156 High Street, Santa Cruz, California 95064, USA. E-mail: shaowei@ucsc.edu*

†Electronic supplementary information (ESI) available. See DOI: 10.1039/c8nr10353d

‡These authors contributed equally to this work.

been found to form strong chemical bonds with lithium polysulfides, which can significantly improve the long-term cycling performance of LSB.[35,36] Of these, MnO_2-based nanocomposites with a uniform structure and large surface area have been attracting particular attention.[37] For instance, Nazar and coworkers dispersed sulfur onto the surface of MnO_2 nanosheets[38] to improve the electrochemical performance. In another study, Chen's group decorated hollow sulfur nanospheres with MnO_2 nanosheets.[39] Diao and coworkers synthetized unique sulfur/γ-MnO_2 core–shell nanocomposites.[40] However, the electrical conductivity of these metal–oxide materials is typically low, in comparison with carbon and conductive polymers, which compromises the rate capability and specific capacity of LSB. Consequently, conductive additives are generally added to the cathode materials.[41] This inevitably reduces the mass loading of active sulfur.

Therefore, it can be envisaged that nanocomposites based on the combination of conductive matrices and polar metal oxides may serve as effective host materials of sulfur. For instance, Lou and coworkers fabricated carbon layer encapsulated titanium monoxide[42] and hollow carbon nanofibers filled with MnO_2 nanosheets to host sulfur nanoparticles,[43] the carbon modified metal oxides composites improved the electric conductivity of sulfur for high capacity and which were effectively to tie the lithium-polysulfides for prolonged cycle life. Kong's group used hollow MnO_2 nanospheres with a PPy shell to encapsulate sulfur, which exhibited an excellent cycling performance.[44] Yu's group also synthesized PPy-MnO_2 nanotubes as a sulfur host for high-performance lithium sulfur batteries.[45]

In this work, we prepared PPy-modified MnO_2 nanotubes for effective encapsulation of sulfur nanoparticles. The MnO_2 nanotubes were synthesized through a facile hydrothermal method and the PPy layer was formed *in situ* by using the MnO_2 as the oxidant. Sulfur nanoparticles were then melted and diffused into the nanotubes. The resulting ternary structure exhibited at least two advantages. First, the hollow interior of the MnO_2 nanotubes provided a large space for the loading of sulfur particles, and the strong chemical interactions with polysulfides intermediates helped minimize the loss of the active species. Second, the PPy shells efficiently enhanced the electrical conductivity of the cathode materials. These led to a remarkable performance as a LSB cathode material.

2. Experimental section

2.1 Materials and reagents

Pyrrole was used after purification by distillation. Concentrated sulfuric acid (H_2SO_4) and hydrochloric acid (HCl) were purchased from Baiyin Liangyou Chemical Reagents Co., Ltd. Potassium permanganate ($KMnO_4$) were purchased from Guangfu Chemical Reagents Co. Sublimed sulfur (99.95%) was obtained from Aladdin Industrial Corporation.

2.2 Fabrication of PPy-modified MnO_2 nanotube-sulfur composites

As shown in Scheme 1, MnO_2 nanotubes were first prepared by a facile hydrothermal method.[46,47] In brief, 0.658 g of $KMnO_4$ was dissolved in 75 mL of deionized water. Then 1.5 mL of concentrated HCl was added into the solution under magnetic stirring for 15 min at ambient temperature. The solution was then transferred to a 100 mL Teflon-lined stainless autoclave, and heated at 150 °C for 12 h. After being cooled down to room temperature, brown precipitates (MnO_2 nanotubes) were filtered and washed with deionized water and ethanol, and then dried at 60 °C in an oven.

MnO_2-PPy nanotubes were then prepared by using the obtained MnO_2 nanotubes as reactive templates. Experimentally, 0.2 g of the as-prepared MnO_2 nanotubes was dispersed in 1 M HCl solution (50 mL) under sonication. After magnetic stirring for 30 min in an ice bath, pyrrole (79.8 μL or 160 μL) was added to the suspension, and the polymerization was carried out in the ice bath for 12 h. Black precipitates were obtained by centrifugation, washed with deionized water and ethanol several times, and then dried at 60 °C, the obtained samples was named MnO_2-PPy and MnO_2-PPy-1, respectively.

The obtained MnO_2-PPy nanotubes were then homogeneously blended with sulfur as a mass ratio of 3 : 7, and the mixture was heated at 155 °C for 24 h in a nitrogen atmosphere, such that sulfur was melted and infiltrate the hollow interiors of the MnO_2-PPy nanotubes. To remove sulfur on the outside surface of the MnO_2-PPy nanotubes, the sample was heated at 200 °C for 2 h. The resulting sample was referred to as MnO_2-PPy-S.

2.3 Characterization

The surface morphology of the as-prepared nanocomposites was examined with a scanning electron microscope (SEM,

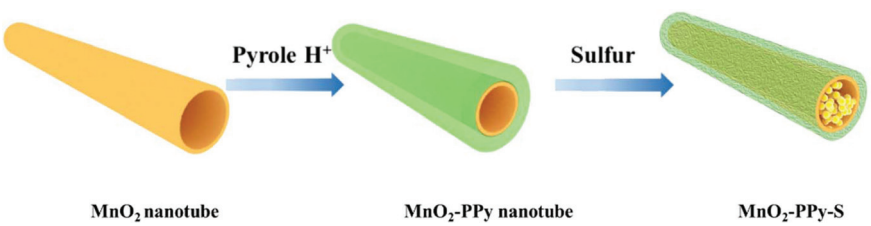

Scheme 1 Schematic illustration of the fabrication of PPy modified MnO_2 nanotube-sulfur composites.

Hitachi S-4800, Japan) equipped with energy dispersive X-ray spectroscopy (EDX), and a high-resolution transmission electron microscope (HR-TEM, JEOL TEM-2010). The sample crystallinity was characterized by using an X-ray diffractometer (XRD, Shimadzu Corp., Kyoto, Japan) with Cu K_α radiation. Thermogravimetric analysis (TGA) (TA Instruments, New Castle, DE) was carried out under a N_2 atmosphere at the heating rate of 10 °C min^{-1}.

2.4 Electrochemical measurement

To prepare working cathodes, the active material obtained above was blended with acetylene black as a conductive agent and polyvinylidenediuoride (PVDF) as binders, at the mass ratio of 8 : 1 : 1, in *N*-methyl-2-pyrrolidone (NMP) to form a uniform slurry. The slurry was cast onto an Al foil current collector and dried at 40 °C for 12 h in a vacuum oven. CR3032 half coin cells were assembled in a glove box filled with argon. Lithium foils were employed as both the counter and reference electrodes, the active material as the cathode and a Celgard 2400 membrane as the separator. The liquid electrolyte was composed of 1 M bis(trifluoromethane) sulfonimide lithium salt (LiTFSI) dissolved in a mixture of 1.3-dioxolane (DOL) and dimethoxymethane (DME) (1 : 1 v : v) with 1% $LiNO_3$ additive. Electrochemical performance was tested at various current densities within the voltage range of 1.7 to 2.8 V *versus* Li^+/Li using a CT2001A battery testing system (LAND Electronic Co.). The electrodes were cycled with a CHI 660E electrochemical workstation in the potential window of 1.7 to 2.8 V *versus* Li^+/Li at the scan rate of 0.1 mV s^{-1}.

3. Results and discussion

3.1 Structural characterization

The MnO_2 nanotube was fabricated and the structure was characterized by SEM and TEM (Fig. 1a, b and Fig. S1†). Obviously, the MnO_2 nanotubes exhibited a smooth surface morphology with an outer diameter of about 85 nm (Fig. S1a†), and clearly hollow tubular interior with an inner diameter of about 50 nm (Fig. 1a and b). The length ranges of

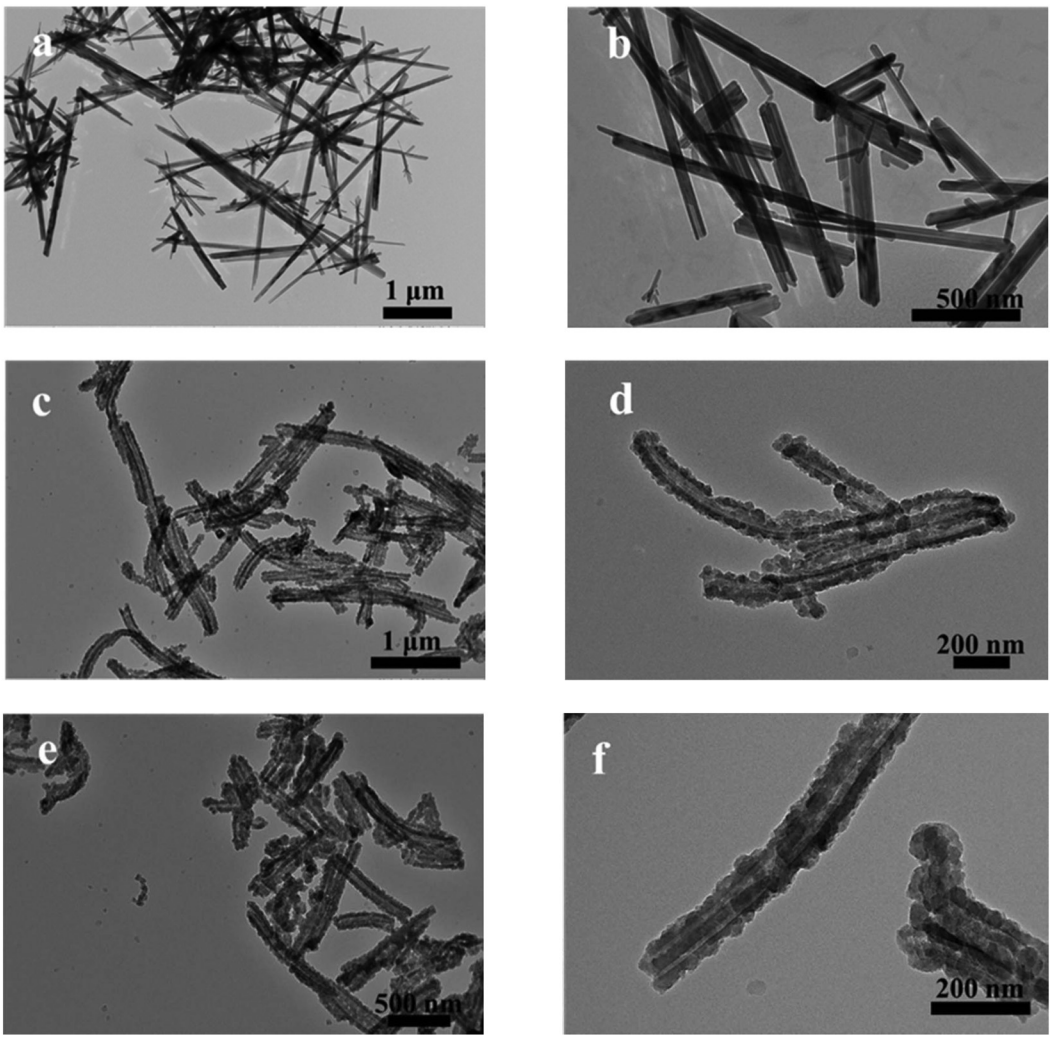

Fig. 1 TEM images of (a, b) MnO_2 nanotubes, (c, d) MnO_2-PPy nanotubes, and (e, f) MnO_2-PPy-S.

MnO_2 nanotube was from several hundreds nanometers to several micrometers characterized by TEM and SEM (Fig. 1a and Fig. S1a†). After the coating of PPy layer, the deposition of PPy nanoparticles rendered the MnO_2 nanotube surfaces drastically roughened, as shown in Fig. S1b and c† and Fig. 1c and d. The formation of this rather compact PPy layer was likely due to the MnO_2 nanotubes that served both as a supporting scaffold and an oxidizing agent for pyrrole polymerization.[48] One can see that in the MnO_2-PPy samples, the hollow nanotube structure was retained, which may be exploited for the loading of sulfur. This can be clearly seen in TEM studies (Fig. 1e and f), whereas no obvious sulfur particles were found on the exterior of the MnO_2-PPy nanotubes (Fig. S1d–f†), suggesting efficient confinement of sulfur within the MnO_2 nanotubes. Indeed, EDS mapping analysis (Fig. 2) shows that the elements of carbon, nitrogen, oxygen, sulfur and manganese were uniformly distributed throughout the sample, indicating the successful and homogeneous loading of PPy and sulfur into the MnO_2 nanotubes. Furthermore, XPS was used to evaluate the change of the samples in the fabrication process. The survey XPS spectra of MnO_2 nanotubes, MnO_2-PPy nanotubes and MnO_2-PPy-S were presented in Fig. S2.† After coating with the PPy, the disappearance of peaks of MnO_2 ($Mn_{2p3/2}$ and $Mn_{2p1/2}$) indicates the introducing of PPy outer layer. In addition, the appearance of characteristics peaks of C 1s and N 1s also prove the existence of PPy layer. Furthermore, the MnO_2-PPy-S discloses the presence of S (S_{2p} and S_{2s}), which exhibits that the S is successfully introduced into the MnO_2-PPy-S nanocomposite sample.

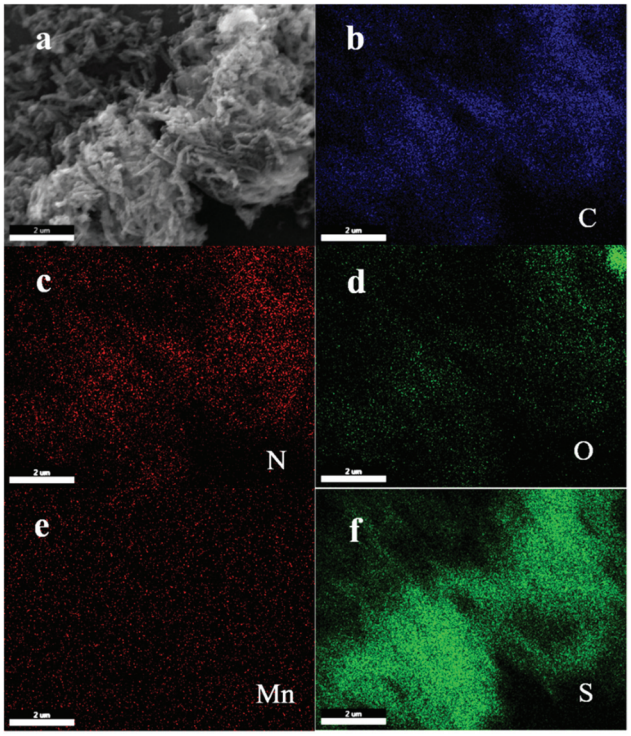

Fig. 2 (a) SEM image of MnO_2-PPy-S and the corresponding elemental maps of (b) carbon, (c) nitrogen, (d) oxygen, (e) manganese and (f) sulfur. Scale bars 2 μm.

The crystalline structures of the samples were then examined by XRD measurements. As shown in Fig. S3,† MnO_2 nanotubes exhibited a series of well-defined diffraction peaks at 12.6°, 18.1°, 28.8°, 37.6°, 41.9°, 49.9°, 56.2°, 60.2°, 65.1° and 69.7°, which can be ascribed, respectively, to the (110), (200), (310), (211), (301), (411), (521), (002) and (541) crystal planes of tetragonal-like α-MnO_2 (JCPDS no. 44-0141); whereas MnO_2-PPy shows only a featureless profile except for a broad peak at *ca.* 24.4°,[49] suggesting an amorphous structure of a PPy outer layer. Interestingly, the diffraction patterns of the MnO_2-PPy-S composite were dominated by those of sulfur, likely because of the high loading of sulfur.

Consistent results were obtained in FT-IR measurements. From Fig. S4,† it is obvious that MnO_2-PPy exhibited a spectral profile consistent with that of PPy, indicating that the MnO_2 nanotubes were well coated with PPy layers. The characteristic bands at 1550 cm^{-1} and 1458 cm^{-1} can be ascribed to the fundamental vibrations of the polypyrrole ring, the bands at 1290 cm^{-1} and 1045 cm^{-1} are due to the C–H in-plane vibrations, and the band at 1180 cm^{-1} arises from the C–N stretching vibration of the polypyrrole chain.[48–50] Interestingly, after sulfur loading, these vibrational features became less well-defined for the MnO_2-PPy-S sample.[51]

The loading of sulfur in the MnO_2-PPy-S composite was then quantitatively evaluated by TGA measurements. From Fig. 3, one can see that the weight loss of the MnO_2-PPy-S sample commenced at *ca.* 180 °C, and the sample weight remained virtually unchanged at temperatures over *ca.* 310 °C. This profile is very similar to that of pure sulfur, whereas PPy was rather stable within this temperature range. The total weight loss for MnO_2-PPy-S was estimated to be 63.5%. That is, sulfur accounts for about 63.5% of the MnO_2-PPy-S sample weight. The MnO_2 content of MnO_2-PPy nanotube was determined to be 16.9% by TGA curve in air atmosphere (Fig. S5†). The adsorption ability of MnO_2-PPy nanotube and MnO_2 nanotube was tested by adding 30 mg of these samples in 2 mL of 0.5 mM L_2S_6 solution (dioxolane/dimethoxyethane, 1 : 1 in volume). Photos of Li_2S_6 adsorption test were presented in Fig. 3b. Obviously, the solution became completely colorless indicating that the MnO_2 nanotube showed excellent adsorption ability for polysulfides. In addition, a very light yellow color in the solution also demonstrated the remarkable polysulfide adsorption ability of MnO_2-PPy nanotube.

N_2 adsorption–desorption measurements were then carried out to quantify the specific surface area and pore structure of the MnO_2-PPy and MnO_2-PPy-S nanocomposites. From Fig. 4a, it can be seen that all samples exhibited type IV adsorption isotherms, indicative of the formation of mesoporous structures. The BET surface area of the MnO_2 nanotube was calculated to be 21.70 $m^2\ g^{-1}$. However, the BET surface area of MnO_2-PPy increased to be 111.51 $m^2\ g^{-1}$ because of the inside diameter enlargement resulted by removal of part of MnO_2 and the rough structure of polypyrrole. The value diminished markedly to 21.46 $m^2\ g^{-1}$ for MnO_2-PPy-S as sulfur impreg-

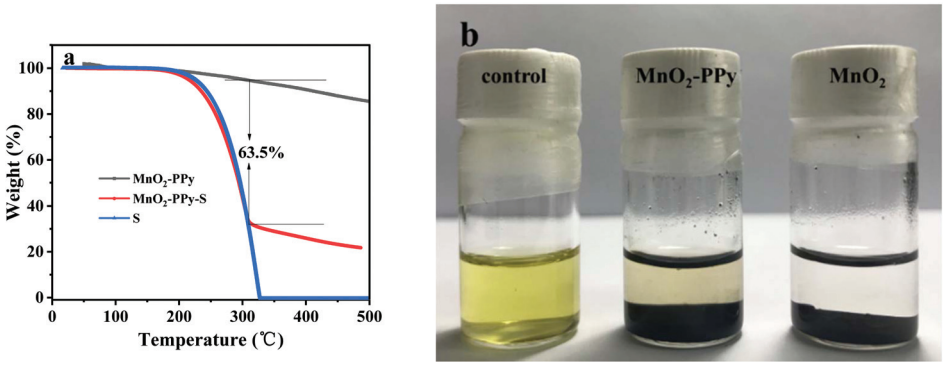

Fig. 3 (a) TGA curves of MnO_2-PPy nanotube, pure sulfur and MnO_2-PPy-S, and (b) photos of Li_2S_6 adsorption test *via* MnO_2-PPy nanotube and MnO_2 nanotube.

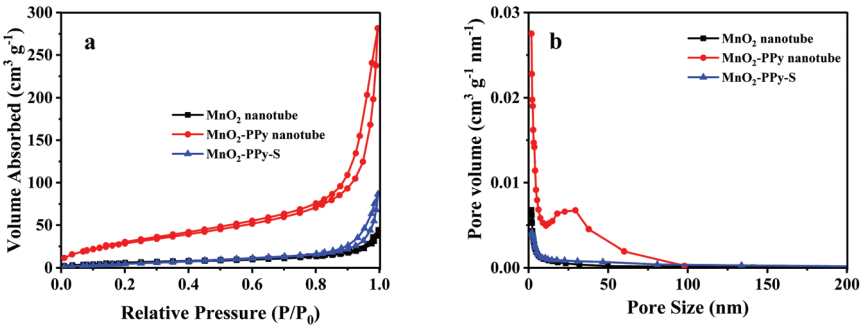

Fig. 4 (a) N_2 adsorption–desorption isotherms and (b) size distribution of MnO_2 nanotube, MnO_2-PPy and MnO_2-PPy-S.

nated the MnO_2 hollow tubes. The mesoporous size distributions of the samples were also affected and the results were presented in Fig. 4b. The MnO_2 nanotube exhibited a pore volume of 0.07 $cm^2\ g^{-1}$ with an average pore size of 11.61 nm. The MnO_2-PPy showed a pore volume of 0.44 $cm^2\ g^{-1}$ with an average pore size of 13.87 nm, while after sulfur loading, the MnO_2-PPy-S sample displayed a substantial decrease of the pore volume to 0.13 $cm^2\ g^{-1}$, whereas the average pore size increased to 19.16 nm, likely because smaller pores were easier to fill up with sulfur impregnation.

3.2 Electrochemical performance

The performance of the MnO_2-PPy-S composite as a cathode material for LSB was then evaluated electrochemically. Fig. 5a shows the charging–discharging cycling performance of the sample at different current densities. The electrode was first cycled at a low current density of 0.05C for activation and then charged and discharged at the current density of 0.2C and 0.5C, respectively. After activation for three cycles, the cathode delivered a specific capacity of 973.8 mA h g^{-1} at 0.2C and 770.4 mA h g^{-1} at 0.5C, respectively; and after 100 cycles, the capacity remained promising at 734.6 and 572.8 mA h g^{-1}.

To evaluate the rate capability of the MnO_2-PPy-S composites, the electrode was charged and discharged from 0.2C to 0.5C, 1C, 2C, 3C and finally back to 0.2C at the voltage range of 1.7 V–2.8 V, as shown in Fig. 5c. The initial specific discharge capacity was 803.3 mA h g^{-1} at 0.2C, and then decreased slowly to 708.0 mA h g^{-1} at 0.5C, 615.3 mA h g^{-1} at 1C, 542.0 mA h g^{-1} at 2C, and 470.0 mA h g^{-1} at 3C. More importantly, the electrode was able to deliver a specific capacity of 726.6 mA h g^{-1} when the current density was re-increased to 0.2C, more than 90% retention as compared to the initial specific capacity. This suggests high reversibility of the operation.

The durability of the MnO_2-PPy-S electrode was further examined by charging and discharging at the current density of 0.2C for 500 cycles. From Fig. 5b (left *y* axis), one can see that during the initial activation at 0.05C, the electrode delivered a specific capacity of 1469.2 mA h g^{-1} in the first cycle. Then as the current density increased to 0.2C, the specific discharge capacity diminished to 973.8 mA h g^{-1} in the 4th cycle. In the following cycles, the discharge capacity declined much more slowly to 734.6 mA h g^{-1} in the 100^{th} cycle, 694.8 mA h g^{-1} in the 200^{th}, 671.9 mA h g^{-1} in the 300^{th}, and 632.1 mA h g^{-1} in the 400^{th} cycle and remained almost invariant at around 586 mA h g^{-1} after the 500^{th} cycle. This means that on average there was only 0.07% capacity decay per cycle during this discharge–charge process (Fig. 5b). Consistent behaviors can be observed with the corresponding coulombic efficiency (Fig. 5b, right *y* axis), where the MnO_2-PPy-S electrode can be seen to demonstrate an outstanding coulombic efficiency of 95.7% on average. As shown in Fig. 5e, the durability of the MnO_2-PPy-S,

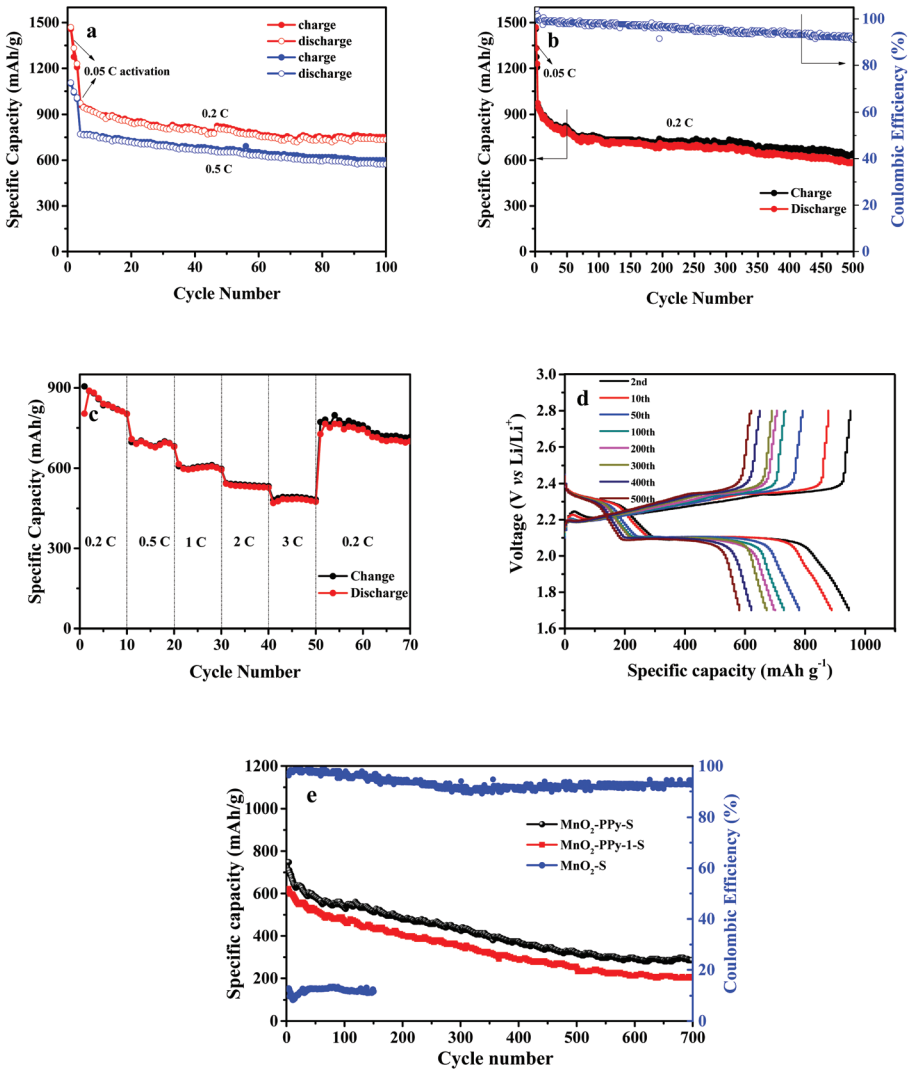

Fig. 5 (a) Cycling stability of MnO_2-PPy-S at 0.2C-rate and 0.5C-rate (b) cycling capacity at 0.2C-rate and the corresponding coulombic efficiency of the MnO_2-PPy-S composites, (c) rate capacities of the MnO_2-PPy-S composites of the MnO_2-PPy-S composites at different current densities, (d) cycling charge–discharge profiles of MnO_2-PPy-S composites at 0.2C rate. (e) Cycling stability of MnO_2-PPy-S, MnO_2-PPy-1-S, MnO_2-S at 0.625C-rate.

MnO_2-PPy-1-S (14.5% MnO_2 content), and MnO_2-S electrodes were further investigated by charging and discharging at the current density of 0.625C for 700 cycles. Obviously, the MnO_2-PPy-S electrode exhibited optimal performance, and possessed the highest specific discharge capacity at 748.1 mA h g^{-1}. Then, the discharge capacity declined much more slowly to about 286 mA h g^{-1} after the 700th cycle. As a result, there was only 0.088% capacity decay per cycle during the discharge–charge process, and the corresponding coulombic efficiency was about 93.4% on average. Compared to the MnO_2-PPy-S electrode, the MnO_2-S achieved very low specific discharge capacity (154 mA h g^{-1}) due to the low conductivity of MnO_2 material. The introduction of PPy layer can improve the electric conductivity of sulfur for high capacity.

In order to investigate the influence of cycling process on the MnO_2-PPy-S cathode, the morphology of MnO_2-PPy-S cathodes before and after 100 cycles at 0.5C-rate are characterized by SEM and TEM (Fig. 6). After 100 cycles, the sulfur remained wrapped in inner of the MnO_2-PPy, and no significant sulfur agglomerates existed on the surface of MnO_2-PPy (Fig. 6a and c), the morphology of the MnO_2-PPy-S after 100 cycles also remained the similar structure with the MnO_2-PPy-S before cycles (Fig. 6b and d).

To evaluate the electrochemical reaction mechanism, the MnO_2-PPy-S cathode was tested by cyclic voltammetric measurements at the scan rate of 0.1 mV s^{-1} from 1.7 V to 2.8 V for 5 cycles. From Fig. 7a, the electrode was swept from open circuit voltage (OCV) to 1.7 V, where element sulfur was reduced to Li_2S_2/Li_2S. Notably, the Li_2S_2/Li_2S species were not oxidized back to element sulfur during the charging process.[51] Two well-defined cathodic peaks appeared at *ca.* 2.3 V (peak i) and 2.1 V (peak ii), which might be ascribed to the reduction

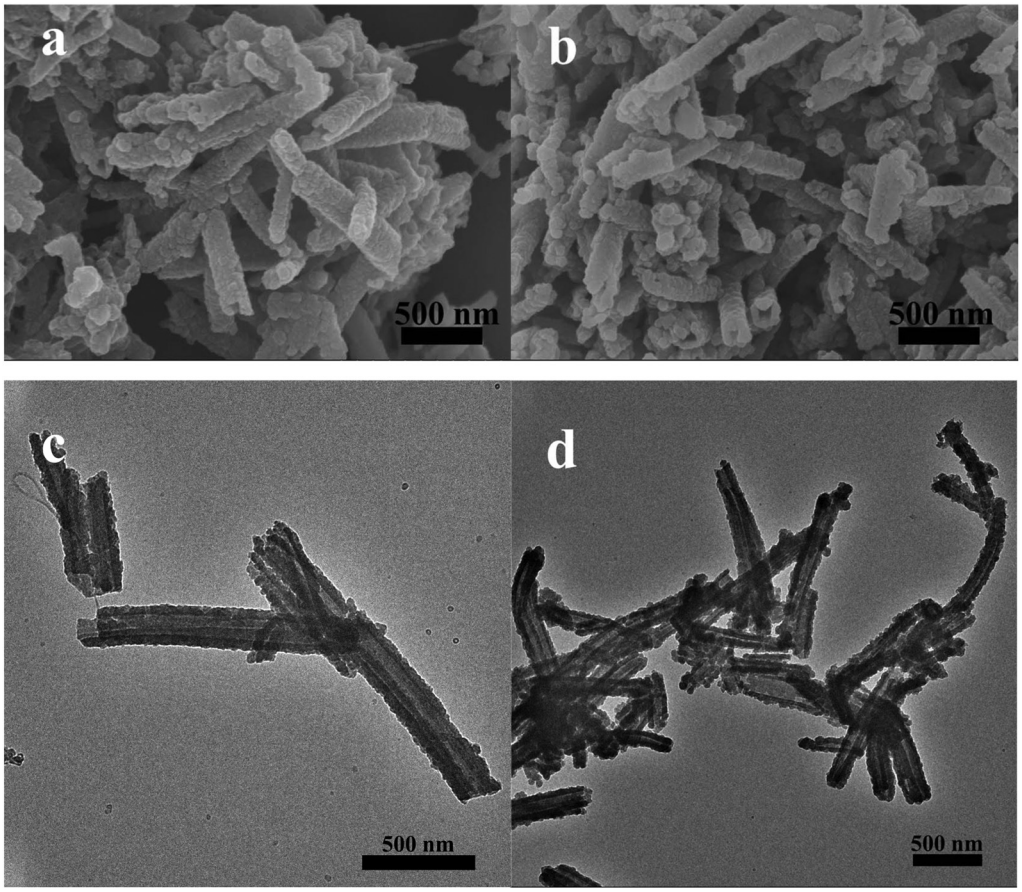

Fig. 6 SEM images of MnO_2-PPy-S after 100 cycles at 0.5C (a) before the cycling (b), and TEM images of MnO_2-PPy-S after 100 cycles at 0.5C (c) before the cycling (d).

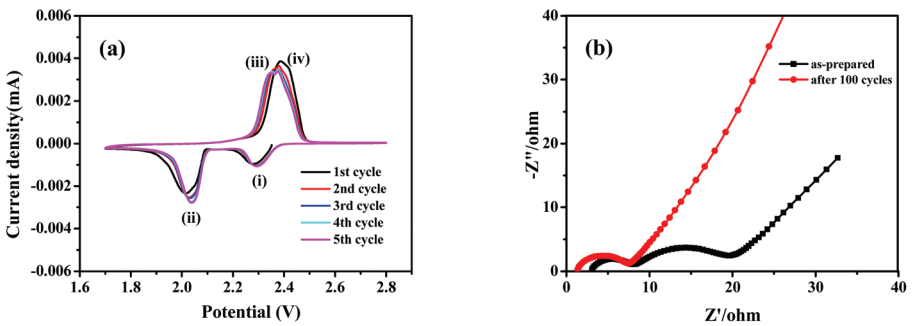

Fig. 7 (a) Cyclic voltammograms of the MnO_2-PPy-S composites at the scan rate of 0.1 mV s^{-1}. (b) Nyquist plots of the MnO_2-PPy-S composites before and after 100 cycles.

of high-order lithium polysulfides (*e.g.*, Li_2S_8) to the low-order species (Li_2S_x. $4 \leq x \leq 8$), and the transformation of soluble lithium polysulfides to solid Li_2S_2/Li_2S, respectively.[24,44] In the corresponding anodic scan, two adjacent peaks can be identified at 2.3 V (peak iii) and 2.4 V (peak iv), likely due to the conversion of the Li_2S_2/Li_2S to low-order lithium polysulfides and then to high-order polysulfides, respectively.[40] In the following four cycles, the voltammograms overlapped with each other, demonstrating good cycling stability of the electrode.

Electrochemical impedance measurements of the MnO_2-PPy-S electrode were then performed to examine the reaction dynamics for lithium insertion and extraction during the cycling tests. The Nyquist plots are depicted in Fig. 7b. It can be seen that the sample exhibited two depressed semicircles in the high and middle frequency domains and a short inclined line in the low frequency domain. The semicircle in the high frequency region can be ascribed to the interfacial charge transfer while the semicircle in the middle frequency region is

Table 1 Electrochemical performance of MnO_2/S cathodes of lithium sulfur batteries

Cathode material	Sulfur content	Cycling stability	Ref.
Hollow PPy-MnO_2-S	74.25%	714 mA h g^{-1} at 0.2C after 200 cycles	44
PPy-MnO_2-S	70%	985 mA h g^{-1} at 0.2C after 200 cycles	45
rGO-MnO_2-S aerogel	67%	886.7 mA h g^{-1} at 0.2C after 200 cycles	53
Hollow carbon nanoboxes-MnO_2-S	67.9%	496 mA h g^{-1} at 4 A g^{-1} after 200 cycles	54
MnO_2/CMK-S	73.4%	600 mA h g^{-1} at 0.1C after 100 cycles	55
Carbon nanofibers-δMnO_2-S	70%	856.1 mA h g^{-1} at 0.5C after 200 cycles	56
S@MnO_2@GO	52%	502 mA h g^{-1} at 0.6 A g^{-1} after 400 cycles	57
PPy-MnO_2 nanotubes-S	63.5%	586 mA h g^{-1} at 0.2C after 500 cycles	This work

likely caused by mass transport for the formation of solid polysulfides (Li_2S and Li_2S_2), which disappeared in the subsequent cycles as the Li_2S_2/Li_2S were not converted back to element sulfur, consistent with results from the CV measurements (Fig. 7a).[40,51,52] Meanwhile, the typical Nyquist plots after 100 cycles exhibited a depressed semicircle in the high frequency region and an inclined line in the low frequency region, which likely reflected the charge-transfer resistance of the interface between the electrolyte and sulfur electrode and the lithium ion semi-infinite diffusion, respectively.

In addition, the resulting MnO_2-PPy-S cathodes demonstrated a remarkable long cycling stability (586 mA h g^{-1} after 500 cycles), rate capability (470 mA h g^{-1} at 3C) and coulombic efficiency (average 95.7%) due to the fine structural combination of metal oxides (MnO_2) and conducting polymer (PPy) which accommodate the volumetric changes and confine the soluble polysulfides. The electrode performance was higher than leading results reported in recent literature (Table 1).

4. Conclusion

In this study, a functional nanocomposite was prepared where polypyrrole modified MnO_2 nanotubes were used as a host scaffold for the impregnation of sulfur. The resulting composites showed a high-performance as the cathode material for lithium sulfur batteries, featuring high specific capacity, excellent cycling stability and good rate capabilities. This was ascribed to the hollow interior of the MnO_2 nanotubes that accommodated the high loading and large volumetric expansion of sulfur particles, and the polypyrrole layer that facilitated charge transfer during the charging–discharging processes.

Conflicts of interest

There are no conflicts to declare.

Acknowledgements

This work was supported by the Fundamental Research Funds for Central Universities (Grant No. lzujbky-2017-99) and the Natural Science Foundation of Gansu Province (Grant No. 1606RJYA249). S. W. C. acknowledged support by the US National Science Foundation (CHE-1710408 and CBET-1848841). W. L. W. was supported by a research fellowship from the China Scholarship Council.

Notes and references

1 L. Ma, K. E. Hendrickson, S. Wei and L. A. Archer, *Nano Today*, 2015, **10**, 315–338.
2 G. Xu, B. Ding, J. Pan, P. Nie, L. Shen and X. Zhang, *J. Mater. Chem. A*, 2014, **2**, 12662–12676.
3 P. G. Bruce, S. A. Freunberger, L. J. Hardwick and J.-M. Tarascon, *Nat. Mater.*, 2011, **11**, 19.
4 X. Ji and L. F. Nazar, *J. Mater. Chem.*, 2010, **20**, 9821–9826.
5 L. Li, J. Yu, N. Wang, J. Zhao, B. Fan, S. Zeng and S. Chen, in *Inorganic Battery Materials*, Wiley, 2018.
6 R. Fang, S. Zhao, Z. Sun, D.-W. Wang, H.-M. Cheng and F. Li, *Adv. Mater.*, 2017, **29**, 1606823.
7 S. Zeng, L. Li, L. Xie, D. Zhao, N. Zhou, N. Wang and S. Chen, *Carbon*, 2017, **122**, 106–113.
8 S. Zeng, L. Li, D. Zhao, J. Liu, W. Niu, N. Wang and S. Chen, *J. Phys. Chem. C*, 2017, **121**, 2495–2503.
9 S.-H. Chung and A. Manthiram, *Adv. Mater.*, 2014, **26**, 1360–1365.
10 Z. Wang, Y. Dong, H. Li, Z. Zhao, H. Bin Wu, C. Hao, S. Liu, J. Qiu and X. W. Lou, *Nat. Commun.*, 2014, **5**, 5002.
11 J.-Q. Huang, T.-Z. Zhuang, Q. Zhang, H.-J. Peng, C.-M. Chen and F. Wei, *ACS Nano*, 2015, **9**, 3002–3011.
12 X. Liang, Z. Wen, Y. Liu, M. Wu, J. Jin, H. Zhang and X. Wu, *J. Power Sources*, 2011, **196**, 9839–9843.
13 S. Liu, G.-R. Li and X.-P. Gao, *ACS Appl. Mater. Interfaces*, 2016, **8**, 7783–7789.
14 Z. Li, Y. Huang, L. Yuan, Z. Hao and Y. Huang, *Carbon*, 2015, **92**, 41–63.
15 W. Li, Q. Zhang, G. Zheng, Z. W. Seh, H. Yao and Y. Cui, *Nano Lett.*, 2013, **13**, 5534–5540.
16 K. Xi, S. Cao, X. Peng, C. Ducati, R. Vasant Kumar and A. K. Cheetham, *Chem. Commun.*, 2013, **49**, 2192–2194.
17 B. Ding, C. Yuan, L. Shen, G. Xu, P. Nie, Q. Lai and X. Zhang, *J. Mater. Chem. A*, 2013, **1**, 1096–1101.
18 R. Chen, T. Zhao, J. Lu, F. Wu, L. Li, J. Chen, G. Tan, Y. Ye and K. Amine, *Nano Lett.*, 2013, **13**, 4642–4649.
19 H. Wang, Y. Yang, Y. Liang, J. T. Robinson, Y. Li, A. Jackson, Y. Cui and H. Dai, *Nano Lett.*, 2011, **11**, 2644–2647.

20 C. Zu, Y. Fu and A. Manthiram, *J. Mater. Chem. A*, 2013, **1**, 10362–10367.
21 N. Jayaprakash, J. Shen, S. S. Moganty, A. Corona and L. A. Archer, *Angew. Chem., Int. Ed.*, 2011, **50**, 5904–5908.
22 X.-B. Cheng, J.-Q. Huang, Q. Zhang, H.-J. Peng, M.-Q. Zhao and F. Wei, *Nano Energy*, 2014, **4**, 65–72.
23 J. Guo, Y. Xu and C. Wang, *Nano Lett.*, 2011, **11**, 4288–4294.
24 W. Wei, P. Du, D. Liu, Q. Wang and P. Liu, *Nanoscale*, 2018, **10**, 13037–13044.
25 Y. Sun, S. Wang, H. Cheng, Y. Dai, J. Yu and J. Wu, *Electrochim. Acta*, 2015, **158**, 143–151.
26 H. Li, M. Sun, T. Zhang, Y. Fang and G. Wang, *J. Mater. Chem. A*, 2014, **2**, 18345–18352.
27 Z. Seh, W. Li, J. J. Cha, G. Zheng, Y. Yang, M. T. McDowell, P.-C. Hsu and Y. Cui, *Nat. Commun.*, 2013, **4**, 1331.
28 X. Liang and L. F. Nazar, *ACS Nano*, 2016, **10**, 4192–4198.
29 W. Li, Z. Liang, Z. Lu, X. Tao, K. Liu, H. Yao and Y. Cui, *Nano Lett.*, 2015, **15**, 7394–7399.
30 Q. Zhang, Y. Wang, Z. W. Seh, Z. Fu, R. Zhang and Y. Cui, *Nano Lett.*, 2015, **15**, 3780–3786.
31 X. Tao, J. Wang, C. Liu, H. Wang, H. Yao, G. Zheng, Z. W. Seh, Q. Cai, W. Li, G. Zhou, C. Zu and Y. Cui, *Nat. Commun.*, 2016, **7**, 11203.
32 C. Dai, L. Hu, M.-Q. Wang, Y. Chen, J. Han, J. Jiang, Y. Zhang, B. Shen, Y. Niu, S.-J. Bao and M. Xu, *Energy Storage Mater.*, 2017, **8**, 202–208.
33 G. Xu, B. Ding, L. Shen, P. Nie, J. Han and X. Zhang, *J. Mater. Chem. A*, 2013, **1**, 4490–4496.
34 H. B. Wu, S. Wei, L. Zhang, R. Xu, H. H. Hng and X. W. Lou, *Chem. – Eur. J.*, 2013, **19**, 10804–10808.
35 X. Liu, J.-Q. Huang, Q. Zhang and L. Mai, *Adv. Mater.*, 2017, **29**, 1601759.
36 S. Rehman, K. Khan, Y. Zhao and Y. Hou, *J. Mater. Chem. A*, 2017, **5**, 3014–3038.
37 S. Wang, Z. Yang, H. Zhang, H. Tan, J. Yu and J. Wu, *Electrochim. Acta*, 2013, **106**, 307–311.
38 X. Liang, C. Hart, Q. Pang, A. Garsuch, T. Weiss and L. F. Nazar, *Nat. Commun.*, 2015, **6**, 5682.
39 X. Wang, G. Li, J. Li, Y. Zhang, A. Wook, A. Yu and Z. Chen, *Energy Environ. Sci.*, 2016, **9**, 2533–2538.
40 L. Ni, Z. Wu, G. Zhao, C. Sun, C. Zhou, X. Gong and G. Diao, *Small*, 2017, **13**, 1603466.
41 J. Zhang, H. Huang, J. W. Bae, S.-H. Chung, W. K. Zhang, A. Manthiram and G. H. Yu, *Small Methods*, 2018, **2**, 1700279.
42 Z. Li, J. Zhang, B. Guan, D. Wang, L.-M. Liu and X. W. Lou, *Nat. Commun.*, 2016, **7**, 13065.
43 Z. Li, J. Zhang and X. W. Lou, *Angew. Chem., Int. Ed.*, 2015, **54**, 12886–12890.
44 Y. Li, B. Shi, W. Liu, R. Guo, H. Pei, D. Ye, J. Xie and J. Kong, *Electrochim. Acta*, 2018, **260**, 912–920.
45 J. Zhang, Y. Shi, Y. Ding, W. Zhang and G. Yu, *Nano Lett.*, 2016, **16**, 7276–7281.
46 J.-G. Wang, Y. Yang, Z.-h. Huang and F. Kang, *Electrochim. Acta*, 2014, **130**, 642–649.
47 J. Luo, H. T. Zhu, H. M. Fan, J. K. Liang, H. L. Shi, G. H. Rao, J. B. Li, Z. M. Du and Z. X. Shen, *J. Phys. Chem. C*, 2008, **112**, 12594–12598.
48 G. Ma, Z. Wen, J. Jin, Y. Lu, K. Rui, X. Wu, M. Wu and J. Zhang, *J. Power Sources*, 2014, **254**, 353–359.
49 C. Wang, W. Wan, J.-T. Chen, H.-H. Zhou, X.-X. Zhang, L.-X. Yuan and Y.-H. Huang, *J. Mater. Chem. A*, 2013, **1**, 1716–1723.
50 X. Liang, M. Zhang, M. R. Kaiser, X. Gao, K. Konstantinov, R. Tandiono, Z. Wang, H.-K. Liu, S.-X. Dou and J. Wang, *Nano Energy*, 2015, **11**, 587–599.
51 Y. Cai, Y. Guo, B. Jiang and Y. Lv, *Sci. Rep.*, 2017, **7**, 14948.
52 Y. V. Mikhaylik and J. R. Akridge, *J. Electrochem. Soc.*, 2004, **151**, A1969–A1976.
53 X. Zhao, H. Wang, G. Zhai and G. Wang, *Chem. – Eur. J.*, 2017, **23**, 7037–7045.
54 S. Rehman, T. Tang, Z. Ali, X. Huang and Y. Hou, *Small*, 2017, **13**, 1700087.
55 J. Liu, C. Wang, B. Liu, X. Ke, L. Liu, Z. Shi, H. Zhang and Z. Guo, *Mater. Lett.*, 2017, **195**, 236–239.
56 Y. Lai, P. Wang, F. Qin, M. Xu, J. Li, K. Zhang and Z. Zhang, *Energy Storage Mater.*, 2017, **9**, 179–187.
57 X. Huang, K. Shi, J. Yang, G. Mao and J. Chen, *J. Power Sources*, 2017, **356**, 72–79.